Application of AVHRR/3 Imagery for the Improved Detection of Thin Cirrus Clouds and Specification of Cloud-Top Phase

KEITH D. HUTCHISON

Center for Remote Environmental Sensing Technology, Lockheed Martin Missiles & Space, Palo Alto, California

(Manuscript received 4 November 1997, in final form 20 December 1998)

ABSTRACT

A multisensor, data fusion technique has been developed that merges the spectral signatures of ice and water clouds in Advanced Very High Resolution Radiometer (AVHRR) imagery with cloud-top pressure analyses derived from the High-Resolution Infrared Sounder (HIRS) to retrieve cloud-top phase and then cloud-top temperatures. While the performance of this algorithm has been encouraging, the specification of cloud-top phase is impacted by the absence of a unique spectral signature for either ice particles or water droplets in AVHRR/2 imagery and the inability to successfully identify very thin cirrus clouds, especially in daytime imagery, with automated cloud detection procedures. With the launch of the AVHRR/3 sensor, new spectral imagery in the 1.6-μm band will ultimately become available, which could help resolve these inadequacies. Thus, the utility of data in the 1.6-μm band is examined for improving the specification of cloud-top phase, while a derived 3.7-μm albedo channel is evaluated for enhancing the automated detection of very thin cirrus clouds in daytime imagery collected over a variety of surfaces. It is concluded that optimal performance of the cloud-top phase algorithm requires the use of both the 1.6- and 3.7-μm bands along with other AVHRR/2 channels. Unfortunately, since these data are not scheduled for simultaneous transmission in the Television Infrared Oberservational Satellite data stream, different implementation strategies are recommended for use with the transmission of the 3.7-μm channel, the 1.6-μm data, and both should they become available in the future.

1. Introduction

The Lockheed Martin Missiles & Space science team has successfully demonstrated a highly accurate, nonlinear, physical relaxation algorithm for the retrieval of moisture profiles from Defense Meteorological Satellite Program (DMSP) SSM/T-2 data. The algorithm has also proven invaluable to advanced sensor design concept studies for future satellite programs (Wilheit et al. 1994). More recently, cloud-top temperatures, derived from a small sample of coincident National Oceanic and Atmospheric Administration (NOAA) AVHRR/2 imagery, have been used successfully as a constraint in this physical relaxation algorithm. Initial results show promise of improved moisture profiles for numerical weather prediction modeling, especially in the presence of nonprecipitating water clouds that have relatively small absorptivities at microwave wavelengths (Wilheit and Hutchison 1997). In general, the accuracy of retrieved moisture profiles are optimal if cloud-top temperatures are precisely known, but little degradation is noted if errors do not exceed about 5°C. The approach also forms the basis for promising new research that has identified a cloud-base spectral signature in microwave moisture sounder data (Wilheit and Hutchison 1999, hereafter WH99; Wilheit and Hutchison 1998).

The accurate specification of cloud-top temperature in Advanced Very High Resolution Radiometer (AVHRR) imagery requires a robust algorithm that must determine cloud-top phase as an intermediate step. If the cloud-top phase analysis identifies only water clouds present in all AVHRR pixels contained within a microwave water vapor sounder pixel, the cloud-top temperature for each AVHRR pixel may be accurately determined from its 10.8-μm brightness temperature that has been corrected for atmospheric attenuation. These retrieved temperatures can then be used with atmospheric profile information, obtained from satellite sounders or numerical models, to determine cloud-top pressures and heights. However, when ice clouds are present (or ambiguity exists in the final cloud-top phase analysis), retrieved cloud-top temperatures are less accurate and moisture profiles may be more accurately analyzed with less reliance on the cloud-top temperature constraint (Wilheit et al. 1994; Wilheit and Hutchison 1997). Additionally, a cloud-base height signature has been identified in simulated microwave water vapor sounder data, but it is only evident when cloud-top temperatures are accurately known (Wilheit and Hutchison 1998; WH99).

Corresponding author address: Dr. Keith D. Hutchison, 769 E. El Camino Real, Ste. 43, Sunnyvale, CA 94087-2919.
E-mail: keith.hutchison@lmco.com

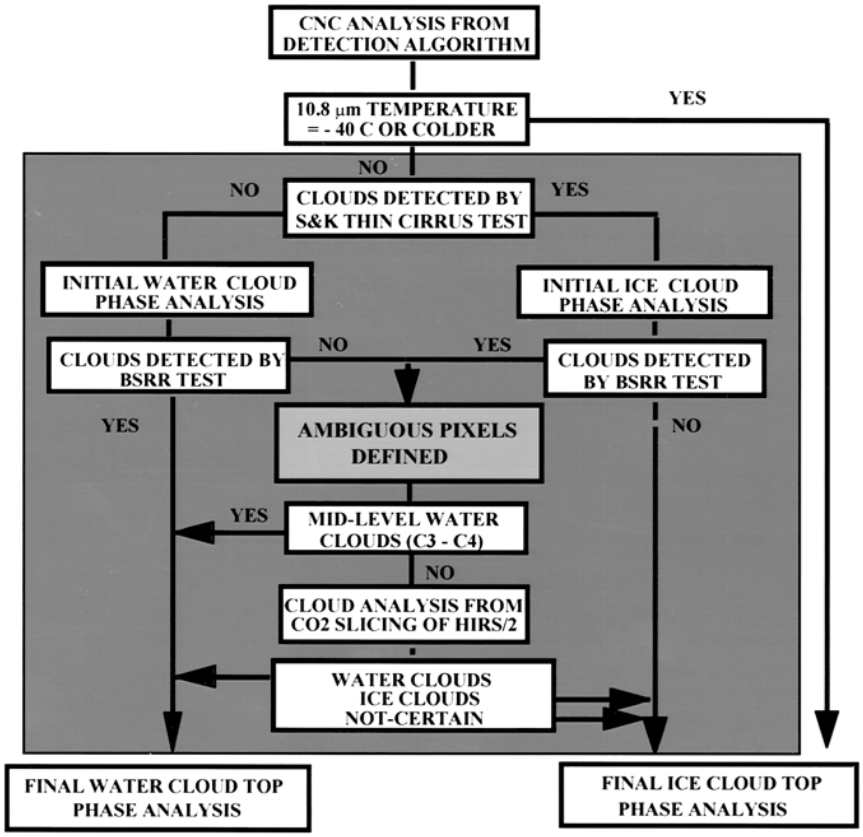

FIG. 1. Cloud-top phase classification algorithm based upon the fusion of spectral signatures in AVHRR imagery and HIRS sounder data (Hutchison et al. 1997b).

Thus, it is critical that the automated cloud detection and cloud-top phase classification algorithms accurately identify and classify *all* thin cirrus in AVHRR/3 imagery to support the accurate retrieval of moisture profiles and possibly cloud-base heights from AMSU-B sounder data.

A multisensor, data fusion technique has been developed to specify cloud-top phase in AVHRR/2 imagery and to assess uncertainty in the final analysis, as shown in Fig. 1 (Hutchison et al. 1997b). The cloud-top phase analysis is initiated from a cloud/no-cloud mask generated by an automated cloud detection algorithm. Ice phase is declared for all pixels in the cloud mask with brightness temperatures at or below $-40°C$ in the 10.8-μm AVHRR channel ($T_{10.8} \leq -40°C$), and these cloudy pixels are classified as unambiguous and placed directly into the final ice cloud-top phase analysis. Cloudy pixels with a brightness temperature greater than $-40°C$ are evaluated by two bispectral tests, that is, the thin cirrus test and the bispectral reflectance ratio (BSRR) test, which were created primarily to detect ice and water clouds, respectively. [The thin cirrus test examines the brightness temperature difference (BTD) between the 10.8- and 12.0-μm channels as a function of the 10.8-μm brightness temperature and sensor scan angle to make cloud/no-cloud decisions (Saunders and Kriebel 1988). The latter test defines cloudy pixels from the ratio between the 0.9- and 0.6-μm channels, that is, BSRR(0.9/0.6), using detection threshold functions that vary with solar illumination, defined by the solar zenith angle, and scattering geometry (Hutchison and Hardy 1995).] All pixels detected by the thin cirrus test are classified as ice in the initial cloud-top phase analysis but considered ambiguous since the test has been shown to detect fractionally cloud-filled pixels containing water clouds (Hutchison and Choe 1996). All pixels not detected by the thin cirrus test are assumed to be water clouds in the initial cloud-top phase analyses.

Pixels in the initial cloud-top phase analyses are then evaluated with the BSRR(0.9/0.6) test. Those in the water cloud-top phase analysis that are detected and those in the ice cloud-top phase analysis not detected by it are classified unambiguous and passed directly into the final water and ice cloud-top phase analyses, respectively. Pixels detected by both the thin cirrus test and the BSRR(0.9/0.6) test, as well as those not detected by either test, are flagged as ambiguous and temporarily classified as ice clouds before undergoing further analysis to ensure that reliable cloud-top temperatures are used in the retrieval of the microwave moisture sounder data. Before applying results from the CO_2 slicing algorithm, all ambiguous pixels are evaluated with a third

bispectral test that examines the BTD between AVHRR/2 channels in the 3.7- and 10.8-μm bands to identify midlevel water clouds that are both highly reflective and relatively cold (Karlsson and Liljas 1990). Since the 3.7-μm channel used in this test contains components of both solar and terrestrial energy, the detection threshold for middle water clouds also varies with solar illumination and scattering geometry and BTDs in the 15°–25°C range are common. This set of results represents the phase of each pixel based *solely* upon the analysis of spectral signatures in the AVHRR imagery and is called the ''intermediate cloud-top phase analyses'' (not shown in Fig. 1).

Results from the CO_2 slicing of High-Resolution Infrared Sounder (HIRS) data are applied to pixels classified as ambiguous in the intermediate cloud-top phase analyses and in effect are used to differentiate between low-level water clouds and high-level cirrus clouds in the AVHRR imagery. Ambiguous pixels with retrieved cloud-top pressures lower than 400 mb are considered ice, while those with pressures higher than 700 mb are considered water. Ambiguous pixels in the intermediate cloud-top phase analysis with cloud-top pressures between 700 and 400 mb remain ambiguous in the final cloud-top phase analyses but remain classified as ice clouds, again to avoid using these less-accurate cloud-top temperatures as a constraint in the retrieval of microwave sounder data. This data fusion technique improves the accuracy of cloud-top phase analyses in the higher-resolution (AVHRR) imagery because the fusion of cloud signatures from the HIRS data is applied at the (cloud) feature level in the AVHRR data, not the resolution of the HIRS pixel (Hutchison et al. 1997b).

While results of the final cloud-top phase classification using this data fusion technique have been encouraging, some difficulties remain (Hutchison et al. 1997b). First, there is no unique spectral signature for either ice particles or water droplets in the existing AVHRR/2 imagery that provides the information content needed to confirm cloud-top phase in daytime imagery. Water and ice cloud optical properties, that is, reflectivities or albedos, lack a unique signature in the 0.6- and 0.9-μm channels, while infrared cloud-top temperatures are insufficient to determine cloud-top phase. In nighttime imagery, the problem only gets worse with the loss of information from both the 0.6- and 0.9-μm bands. Some differences in cloud optical properties do exist between ice and water clouds in the 3.7-μm band of AVHRR/2 data, and these differences have been used successfully with nighttime imagery to retrieve cirrus cloud optical parameters given a priori knowledge of ice cloud phase (Ou et al. 1993, 1995, 1996), while a similar approach has been used with daytime imagery (Rao et al. 1995).

Second, the automated detection of optically thin cirrus is not completely satisfactory in AVHRR/2 imagery using the thin cirrus test (Hutchison et al. 1995; Hutchison and Choe 1996). Difficulties arise because the spectral signatures of ice particles and water vapor are similar in AVHRR/2 infrared bands and differ only in degree. Thus, water vapor may be considered noise in this bispectral approach, which makes it more difficult to detect cirrus clouds as the atmosphere becomes increasingly humid. The problem is magnified over land where variations in surface emissivity further impact the retrieval (Hutchison et al. 1995; Gao et al. 1993). It has been shown that significant improvement is possible in the detection of thin cirrus using 1.38-μm imagery (Hutchison and Choe 1996). While these data should (hopefully) become available on the next generation of meteorological satellites, additional improvement in cloud-top phase specification is needed during the AVHRR/3 era. In the meantime, AVHRR imagery centered near 3.7 μm have been corrected for thermal emissions to create an albedo image in which the contrast between snow and thin cirrus clouds is greatly enhanced for snow mapping (Hutchison et al. 1997a; Hutchison and Locke 1997). These data have not been quantitatively evaluated to determine their utility for improved thin cirrus detection.

Third, it has been noted that cloud-top pressures derived from the CO_2 slicing of HIRS/2 data may erroneously change cloud-top phase classifications of some ambiguous pixels from ice clouds, in the intermediate cloud-top phase analysis, to water clouds in the final analysis (Hutchison et al. 1997b). This occurs primarily because errors in cloud-top pressures are frequently as large as 100 mb in multilayered cloud systems (Menzel and Strabala 1997). Therefore, it becomes desirable to reduce the number of ambiguous pixels in the intermediate ice and water cloud-top phase analyses prior to merging cloud-top pressure analyses from the CO_2 slicing of HIRS data.

Additional research is being pursued in an attempt to improve the accuracy of cloud-top pressures retrieved from HIRS data. Sensitivity studies have been completed to quantify the impact of inaccuracies in the specification of atmospheric parameters on results obtained with the CO_2 slicing algorithm (Huang and Hutchison 1998). Initial results from these studies suggest alternative approaches to improve analyses of cloud-top pressures in HIRS data, including the use of a cloud/no-cloud mask generated by the automated analysis of the AVHRR imagery. An extensive study is currently under way so a complete discussion of this topic is deferred until a later time.

In this paper, the potential value of 3.7-μm albedo data for the enhanced detection of thin cirrus clouds is evaluated along with the applicability of 1.6 μm for reducing ambiguity in the intermediate cloud-top phase analyses of AVHRR/3 imagery. Since the current data transmission schedule for AVHRR/3 imagery calls for the 1.6- and 3.7-μm channels to share the same position in the transmission data stream, both channels will not be available at the same time. The 1.6-μm imagery is currently scheduled for transmission only on the after-

noon satellite (Wrublewski 1996). Therefore, implementation strategies are evaluated for use with the transmission of the 3.7-μm channel, the 1.6-μm data, and both should they both become available in the future.

2. Use of 3.7-μm albedo imagery for the detection and identification of thin cirrus clouds

Figure 2 shows a scene that has been used extensively to study the detection and classification of optically thin cirrus clouds over diverse land backgrounds (Hutchison et al. 1997a,b). Panel A(1) contains the AVHRR 0.9-μm band, while panel A(2) shows the 12.0-μm channel for a *NOAA-12* scene over the western United States collected at 1505 UTC 19 March 1996. The analysis area is approximately a 1000-km square and extends in the north–south direction from near Portland, Oregon, to Los Angeles, California, and from the border of Utah and Nevada to the 130° west meridian in the east–west direction. Major discernible features seen in the 0.9-μm band include snow along the Sierra Nevada and regions to the right, while water clouds over much of the left half of the image appear highly reflective and cumuliform. Thin cirrus is evident from the middle through upper-right corner in the infrared imagery shown in panel A(2) and across much of the bottom third of the scene (Scorer 1990).

a. Thin cirrus detection with the 3.7-μm albedo channel

There are two widely recognized methods used to detect cirrus clouds in daytime AVHRR/2 imagery collected over land surfaces. One method is based upon the brightness temperature of the 10.8-μm AVHRR channel and is used to detect optically thicker cirrus, for example, clouds with a brightness temperature of -40°C or colder, that is, $T_{10.8} \leq -40$°C. The other method is commonly referred to as the thin cirrus test and it is used to detect optically thinner cirrus. As previously noted, the thin cirrus test examines the BTDs between the 10.8- and 12.0-μm channels, as a function of the 10.8-μm temperature and sensor scan angle, to differentiate between atmospheric water vapor and the presence of optically thin cirrus clouds (Saunders and Kriebel 1988). While optically thick cirrus are readily detected, the accurate detection of optically thin cirrus is more difficult, especially over land surfaces (Hutchison and Choe 1996; Hutchison et al. 1995; Gao et al. 1993).

Recent studies have demonstrated that the contrast between thin cirrus clouds and snow can be greatly enhanced in the daytime 3.7-μm imagery by removing the thermal component from the observed radiances and converting the resultant values into albedos to produce an image hereafter referred to as the 3.7-μm albedo (3.7a) channel (Hutchison et al. 1997a). Initially, the 3.7-μm albedo channel was used to differentiate between snow and water clouds and perform land surface classifications (Allen et al. 1990; Gutman 1992). More recently, it has become evident that the 3.7-μm albedo channel, used in conjunction with 0.6-μm imagery, greatly improves the ability to differentiate between very thin cirrus clouds and snow-covered surfaces and even allows snow to be identified through overcast thin cirrus conditions (Hutchison et al. 1997a; Hutchison and Locke 1997). The improved contrast between thin cirrus clouds and snow in the 3.7-μm albedo image greatly assists in generating manual cloud/no-cloud analyses, which is constructed with the aid of special Lockheed Martin proprietary software (Hutchison et al. 1995). A 3.7-μm albedo image create using this procedure is shown in panel B(1). Comparisons between panels A(1) and B(1) reveal that the albedos of the snow-covered pixels are greatly reduced in the 3.7-μm albedo image.

The a priori cirrus cloud analysis for the scene is shown in panel B(2) of Fig. 2. This manual cloud/no-cloud analysis serves as ground truth to quantify the accuracy of similar cloud analyses based upon automated procedures. Manual cloud analyses, based upon human interpretation of clouds in a scene, have proven useful for quantifying the accuracy of cloud analysis and forecast models (Hutchison and Hardy 1995; Hutchison et al. 1995; Hutchison and Janota 1989). In addition, the manual analysis of clouds in multispectral imagery is defined as the basis for demonstrating algorithm performance for cloud detection in both the DMSP Block 6 and NPOESS programs (DMSP 1991; NPOESS 1997). More recently the technique of manually generating cloud/no-cloud analyses has been applied to assessing the performance of cloud-top phase algorithms, with limitations due to ambiguities in ice cloud spectral signatures in AVHRR/2 imagery (Hutchison et al. 1997a).

The automated cirrus analysis of the scene in Fig. 2, based upon the thin cirrus test and the $T_{10.8} \leq -40$°C test, is shown in panel C(1). [Partially cloudy pixels containing water clouds detected by the thin cirrus test were removed for simplicity but are shown later in panel A(2) of Fig. 5.] The a priori ice cloud-top phase analysis contains 223 476 cloudy pixels as shown in panel B(2); these automated cirrus tests detected 141 046 for an accuracy of 63.1% (Hutchison et al. 1997b). Most of the misclassifications occur in the bottom third of the scene. (Inaccuracies results primarily from using the 10.8-μm brightness temperature as a method of estimating atmospheric water vapor absorption—a procedure that works well for maritime atmospheres for which it was developed but naturally more poorly when applied to global conditions.) Too much cirrus has gone undetected in the automated analysis to use the cloud-top temperatures with confidence as a constraint in the retrieval of moisture profiles. Thus, the utility of the 3.7-μm albedo channel is quantitatively evaluated as a means of improving the detection of very thin ice clouds not detected by these more widely known cirrus cloud tests.

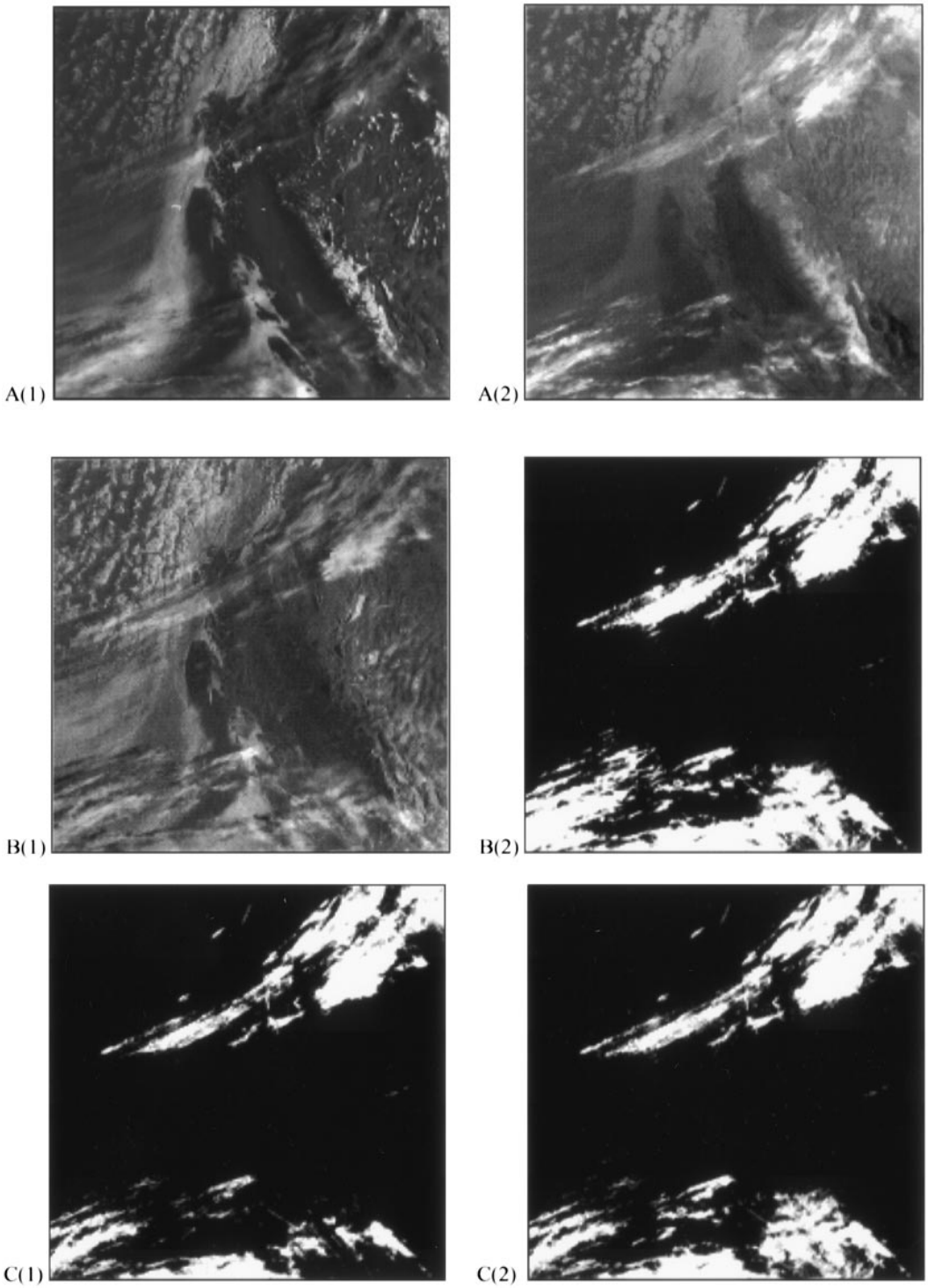

FIG. 2. *NOAA-12* AVHRR imagery collected over western United States at 1505 UTC 19 March 1996. (a) Highly reflective snow, water clouds, and the California coastline are best seen in the AVHRR 0.9-μm band [A(1)], while thin cirrus clouds are generally more discernible in the 12.0-μm band [A(2)]. (b) Contrast between snow (which now appears black), ice clouds, and other features is enhanced in the 3.7-μm albedo data [B(1)], which is very useful in creating the a priori (manual) ice cloud-top phase analysis [B(2)]. (c) Less cirrus is detected using only the $T_{10.8} \leq -40$°C and the thin cirrus tests [C(1)] when compared to results obtained by also including the BSRR(3.7a/0.6) test, shown in C(2), in the automated cirrus detection procedure.

It has been shown by theoretical calculations and with AVHRR/2 imagery that the signature of thin cirrus is stronger in the 3.7-μm albedo channel than in the 12.0-μm channel because cirrus features in the 3.7-μm albedo channel appear very similar to those in a 3.7-μm minus 10.8-μm BTD image (Hutchison et al. 1997a). Since thin cirrus clouds are more apparent in the 12.0-μm than in the 0.6-μm channel, the albedo of thin cirrus cloudy pixels is always larger in the 3.7-μm albedo channel than in the 0.6-μm band, even for low solar zenith angles. Additionally, albedos over cloud-free vegetated land are typically smaller in the 3.7-μm albedo image than in the 0.6-μm band, which forces the BSRR(3.7a/0.6) values to exceed unity when thin cirrus overlies vegetated land and ocean surfaces.

Therefore, the bispectral reflectance ratio between the 3.7-μm albedo channel and 0.6-μm channel, that is, BSRR(3.7a/0.6), appears well suited to detect very thin cirrus over vegetated land and ocean surfaces, which may otherwise go undetected by the thin cirrus test and the $T_{10.8} \leq -40$°C test. The improvement sensitivity in detecting thin cirrus with the BSRR(3.7a/0.6) test may be seen by comparing panels C(2) against the automated analysis shown in panel C(1) of Fig. 2. Including the condition that cirrus are present if BSRR(3.7a/0.6) $>$ 1.0 with the other cirrus tests used to create the automated analysis in panel C(1) improved the accuracy of automated cirrus analysis from 63.1% to 81.7% when compared to the a priori ice cloud-top phase analysis in panel B(2) of Fig. 2. Most of the improvement occurred near the lower-right corner of the scene. (Again, pixels containing water clouds were removed from the analysis for simplicity.) This represents a 29.5% relative improvement, which is gained by incorporating the BSRR(3.7a/0.6) test with results from the thin cirrus test and the $T_{10.8} \leq -40$°C test.

b. Limitations on the use of 3.7-μm albedo imagery for thin cirrus detection

To understand the limitations on the use of 3.7-μm albedo imagery for thin cirrus detection, it is helpful to distinguish between densely vegetated and poorly vegetated land surfaces in this scene. The interpretation of features in multispectral imagery is facilitated by the use of false color composite images, which are made by assigning a different spectral band to each gun of a cathode ray tube (CRT) (d'Entremont et al. 1987). The hue of the false color composite emphasizes the gun in which the feature has the strongest signature. In AVHRR/2 imagery, the signature of thin cirrus is strongest in the 3.7-μm albedo image (daytime) and the 3.7 $-$12.0-μm BTD feature (nighttime), but it is also strong in the 12.0-μm channel (daytime and nighttime). The signature of vegetated land is pronounced in the 0.9-μm channel, while water clouds are similar in both the 0.6- and 0.9-μm channels. Equal contributions from each channel in the CRT results in a feature appearing as a (white through black) gray shade in the false color composite, with the shade of gray depending upon the strength of albedos or brightness temperatures of the feature in the spectral bands.

The false color composites shown in Fig. 3 are useful in identifying areas that are more densely and less densely vegetated in an attempt to understand the limitations of using the 3.7-μm albedo channel for cirrus detection over land surfaces. Densely vegetated land is recognized by the green color shown in the false-color composite in panel A(1), which was created by assigning the 0.6-μm band to the red and blue guns and the 0.9-μm channel to the green gun of the CRT. Sparsely vegetated land appears grayish in this image and is found primarily to the right of the snow-covered mountains, which appear white and extend from the lower-right corner to near the middle of the scene. The sparsely covered region contains much of Nevada and desert areas of California, which are located below and to the right of the mountains. Most water clouds also appear white, which means they have approximately equal spectral signatures in both bands.

The second false-color composite, shown in panel A(2) of Fig. 3, was created by assigning the 0.6-μm band to the red and blue guns and the 3.7-μm albedo channel to the green gun of the CRT. In this color composite, cloud-free densely vegetated land, identified in panel A(1), and ocean surfaces appear dark since they have similar spectral signatures and small albedos in both bands. On the other hand, both sparsely vegetated, cloud-free regions and thin cirrus clouds have a greenish hue due to the higher albedos in the 3.7-μm albedo channel. Thus, it is expected that thin cirrus and sparsely vegetated land features will be indistinguishable with a BSRR(3.7a/0.6) test.

Panel B(1) shows cloud-free pixels in the scene with BSRR(3.7a/0.6) values that exceed unity. As suggested in the false-color composite in panel A(2), these pixels occur primarily over the sparsely vegetated areas located to the right (east) of the snow-covered Sierra Nevada. These regions would be misclassified as thin cirrus if not masked from the BSRR(3.7a/0.6) test; thus, the BSRR(3.7a/0.6) test cannot be used for thin cirrus detection over sparsely vegetated land surfaces. Cloud-free densely vegetated land and ocean surfaces, apparent in panels A(1) and A(2), have BSRR(3.7a/0.6) values that are well below the cirrus detection threshold and do not need to be masked from the test. Panel B(2) of Fig. 3 shows results of using the BSRR(3.7a/0.6) $>$ 1.0 test for all pixels in the scene except those identified as sparsely vegetated in panel B(1).

Additionally, the BSRR(3.7a/0.6) test cannot detect thin cirrus clouds over lower-level water clouds. Panels A(1) and A(2) in Fig. 2 as well as the color composite in panel A(2) of Fig. 3 show the presence of multilayered cirrus and water clouds in the lower-left corner of the scene. Thin cirrus in this area appear both greenish and gray in panel A(2) of Fig. 3. Pixels that appear gray

in the color composite lack a unique spectral signature in either the 3.7-μm albedo or 0.6-μm channels and consequently neither thin cirrus nor water clouds would be detected by the BSRR(3.7a/0.6) test in this region. This is most clearly seen by comparing results from the BSRR(3.7a/0.6) test, in panel B(2) of Fig. 3, with the a priori ice cloud-top phase analysis in panel B(2) of Fig. 2. Much more thin cirrus is contained in the manual ice cloud-top phase analysis than was detected by the BSRR(3.7a/0.6) test in this region of multilayered clouds. In effect, the reflectivity of lower-level water clouds in the 0.6-μm channel overwhelms the smaller signature of ice clouds in 3.7-μm albedo channel, while the complex signature of stratiform clouds is relatively small in the 3.7-μm channel (Scorer 1990). Consequently, the BSRR(3.7a/0.6) test is ineffective at detecting either ice or water clouds when they occur in the same pixel. On the other hand, the thin cirrus test proves more useful for detecting thin cirrus over water cloud layers, as seen by comparing panel B(2) of Fig. 3 and panel C(1) of Fig. 2 with panel B(2) of Fig. 2. [The thin cirrus test detected significantly more thin cirrus in the lower-left corner of the scene than was detected by the BSRR(3.7a/0.6) test.] This makes the BSRR(3.7a/0.6) test a complement to, not a replacement for, the thin cirrus test and the $T_{10.8} \leq -40$°C test.

c. Use of 3.7-μm albedo data for cloud-top phase classifications

Returning to panel A(2) of Fig. 3, it is seen that numerous water clouds and cirrus clouds, not overlying lower-level water clouds, have a greenish hue in the false color composite. Other regions of water clouds have a purple hue and the color differences for water clouds result from the interaction of 3.7-μm energy with the different droplet size distributions associated with cumuliform and stratiform clouds (Scorer 1990). Since the spectral signatures of ice and some water clouds are similar in panel A(2), a BSRR(3.7a/0.6) test should not effectively discriminate between them; thus, the test should not be considered directly useful for cloud-top phase classifications. These expectations are confirmed in results shown in panel B(2) of Fig. 3, where it is evident that the test did detect both cumuliform water clouds in addition to ice clouds.

On a limited basis, it is possible to detect and identify cirrus clouds in pixels classified as cloudy by the BSRR(3.7a/0.6) test, but this may only be done by inference, that is, showing the absence of water clouds. The process of inferring ice cloud-top phase by the absence of water clouds in pixels known to be cloudy is demonstrated in panels C(1) and C(2) of Fig. 3. Because the BSRR(3.7a/0.6) test detects thicker cirrus along with cumuliform water clouds, it becomes highly desirable to differentiate between very thin cirrus detected *uniquely* by the BSRR(3.7a/0.6) test and all other clouds detected by the automated cloud detection algorithm that generated the cloud/no-cloud mask used to initiate the cloud-top phase algorithm. Clouds in the scene detected uniquely by the BSRR(3.7a/0.6) test are shown in panel C(1), which contains 44 620 cloudy pixels. Next, these cloudy pixels are evaluated with the BSRR(0.9/0.6) test, which was developed to be highly sensitive to water clouds. Panel C(2) shows that only 2063 of the 44 620 pixels cloudy pixels in panel C(1) that were also detected as water clouds by the BSRR(0.9/0.6) test. Thus, using similar logic as described in Fig. 1, the vast majority of the 44 620 pixels uniquely detected by the BSRR(3.7a/0.6) test may now be classified unambiguously as ice clouds and entered directly into the final ice cloud-top phase analysis. The remaining 2063 pixels detected by both tests must be considered ambiguous at this time. If these pixels are cirrus clouds, they will likely be classified as glaciated using results from the analysis of HIRS data since the CO_2 slicing algorithm most accurately retrieves cloud-top pressures of thin clouds uniquely detected by the BSRR(3.7a/0.6) test, that is, single layers of thin cirrus not overlying lower-level water clouds (Wylie et al. 1994).

There are several obvious weaknesses in the approach of making ice cloud-top phase classifications based upon the absence of water clouds. First, it is more desirable to positively confirm the presence of ice clouds directly rather than infer their presence indirectly. Second, bispectral reflectance ratio tests, for example, the BSRR(0.9/0.6) test, provide more accurate results with higher-resolution local area coverage (LAC) data than global area coverage (GAC) data. Obviously, partially cloud-filled pixels occur more frequently in GAC than LAC data, and the spectral signature of water clouds in partially cloud-filled pixels may exceed the upper limit of unity for the BSRR(0.9/0.6) test over vegetated surfaces (Saunders and Kriebel 1988; Hutchison and Hardy 1995). Finally, the BSRR(0.9/0.6) test cannot differentiate between cirrus overlying water clouds and only water clouds in the AVHRR sensor field of view; consequently, the absence of ice clouds cannot be concluded by the presence of water clouds.

A modification of the original cloud-top phase algorithm, described in Fig. 1, to more fully exploit the information content of the 3.7-μm albedo channel for the improved detection of very thin cirrus over land surfaces is shown in Fig. 4. Key to this modified approach is the identification of all thin cirrus clouds uniquely detected by the BSRR(3.7a/0.6) test. The application of this test requires a surface vegetation classification to ensure that cloud-free, nonvegetated, or sparsely vegetated surfaces are not misanalyzed as thin cirrus clouds. All pixels uniquely detected by the BSRR(3.7a/0.6) test can be entered into the initial ice cloud phase analysis, where ice phase is confirmed by the absence of water clouds. While some misclassifications will occur, as seen in panel C(2) of Fig. 3, these should be small in number and may yet be recovered using cloud-top pressures retrieved by the CO_2 slicing

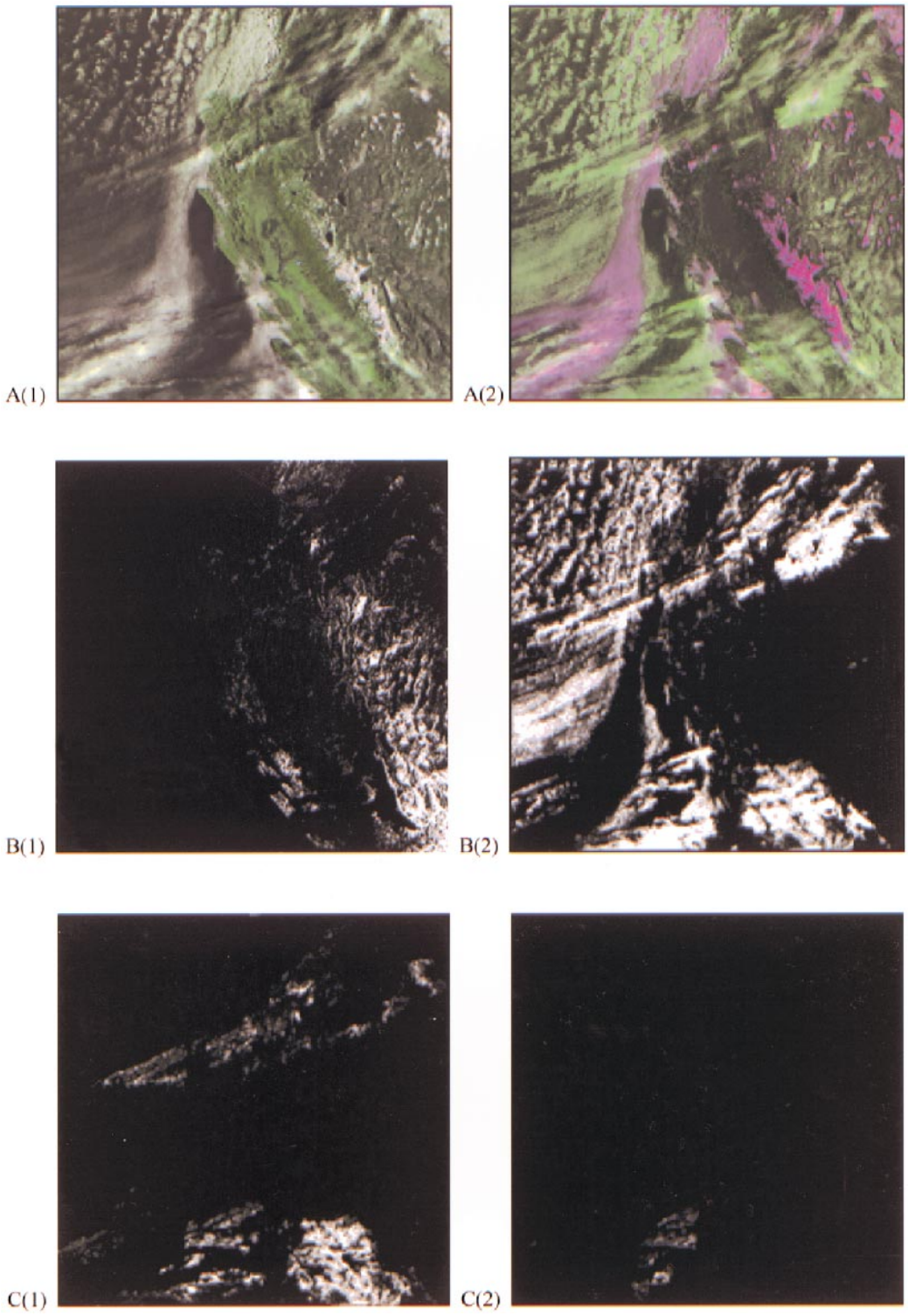

FIG. 3. Analysis of surface and cloud spectral signatures in the 19 March 1996 scene. (a) More densely vegetated land appears greenish in the color composite at A(1), made by assigning the 0.6-μm band to the red and blue guns and the 0.9-μm band to the green gun of the CRT, while sparsely vegetated land appears gray, to right of the snow-covered mountains. This sparsely vegetated land, thin cirrus, and many water clouds all have the same (greenish hue) spectral signature in the false-color composite shown in A(2), where the 0.9-μm channel is replaced with the 3.7-μm band. (b) Cloud-free, sparsely vegetated land would be misclassified as clouds by the BSRR(3.7a/0.6) test used todetect thin cirrus [B(1)], which restricts the test to more densely vegetated land and ocean areas. Once these sparsely vegetated areas are masked, the BSRR(3.7a/0.6) test is found to detect both water clouds and ice clouds [B(2)], but

algorithm with HIRS data. This implementation is useful with and without 1.6-μm data.

3. The value of 1.6-μm imagery for cloud-top phase specification

The new AVHRR/3 sensor will have the capability to transmit data in the 1.6-μm band, although these data may not be routinely available with NOAA-K due to its early morning orbit. Nevertheless, this channel contains the only spectral data not currently available with the AVHRR/2 sensor. It is hoped that 1.6-μm data can be used to further reduce the ambiguities in the intermediate cloud-top phase analyses, which must be resolved using cloud-top pressures retrieved from the CO_2 slicing of HIRS sounder data.

As previously mentioned, the thin cirrus test may detect partially cloud-filled pixels containing water clouds in addition to ice clouds present in a scene. Thus, a primary objective of this paper is to report on the usefulness of 1.6-μm imagery for identifying pixels containing these water clouds and remove them from the initial ice cloud-top phase analysis. For example, panel A(1) of Fig. 5 contains the initial ice and water cloud-top phase analyses for the AVHRR/2 scene shown in Fig. 2. (White represents clouds satisfying the condition that $T_{10.8} \leq -40$°C, light gray represents clouds detected by the thin cirrus test, dark gray is assigned to water clouds, and cloud-free pixels are black.) The image shown in panel A(2) contains the water clouds present in the initial ice cloud-top phase analysis that were detected by the thin cirrus test. It is hoped that the 1.6-μm data will prove useful in removing similar misclassified pixels from the initial ice cloud-top phase analysis of AVHRR/3 imagery.

Panels A(1) and A(2) of Fig. 6 show 0.6- and 1.6-μm images, respectively, for data collected by the Airborne Visible/Infrared Imaging Spectrometer (AVIRIS) sensor flown aboard a National Aeronautics and Space Administration ER-2 aircraft over the Gulf of Mexico during December 1990 (Vane 1987). These data have a nominal horizontal resolution of 20 m. The 1.38-μm image is shown in panel B(1) to emphasize the location of thin cirrus clouds in the scene, while the a priori (manual) ice cloud-top phase analysis is shown in panel B(2). Not shown is the automated analysis of all clouds in the multispectral imagery, but it is available in the literature (Hutchison and Choe 1996).

Water clouds are highly reflective in the 0.6-, 0.9-, and 1.6-μm channels and their presence may be confirmed using a bispectral reflectance ratio with any combination of these channels. For example, the automated water analysis, shown in panel C(1) of Fig. 6, was created using a bispectral reflectance ratio test with a threshold function, which varies with solar illumination and scattering angle (Hutchison and Hardy 1995). However, in this case the 0.9-μm channel albedos were replaced with data from the 1.6-μm band. For the level of solar illumination and the scattering geometry present in this scene, the automated analysis of water clouds contains pixels with BSRR(1.6/0.6) values in the range of 0.7–1.0. Cloudy pixels are classified as glaciated based upon the condition that BSRR(1.6/0.6) < 0.7 and results are shown in panel C(2).

It is evident by comparing panels B(2) and C(2) of Fig. 6 that reflected energy from lower-level water clouds overwhelms the signature of ice clouds in the 1.6-μm band and causes ice clouds to be misclassified as water clouds. These water clouds are accurately described in the automated water cloud top phase analysis in panel C(1), and their outline is also seen in the ice cloud-top phase analysis at panel C(2). Thus, over surfaces that have a small albedo in the 1.6-μm channel, ice clouds may be confirmed in the automated cloud mask using the BSRR(1.6/0/6) test and a threshold just below the variable threshold range for water clouds described for the BSRR(0.9/0/6) test, for example, 0.7 for this particular case (Hutchison and Hardy 1995). However, cloudy pixels with BSRR(1.6/0/6) values that exceed the lower limit of this variable threshold range remain ambiguous and must be evaluated with cloud-top pressure analyses from HIRS/3 sounder data since it remains possible that thin cirrus may be present in addition to the water clouds. Unfortunately, this means that a primary objective for using 1.6-μm imagery in the cloud-top phase algorithm cannot be satisfied, that is, to identify pixels containing water clouds that were detected by the thin cirrus test and remove them from the initial ice cloud-top phase analysis. The implementation of the logic for using 1.6-μm imagery collected over low (1.6 μm) albedo surfaces is shown in Fig. 7.

A more direct approach to the specification of ice cloud-top phase is desirable but requires additional spectral data not available with the AVHRR/3 sensor. For example, signatures of lower-level water clouds are frequently suppressed in 1.38-μm imagery, as shown in panel B(1) of Fig. 6 (Hutchison and Choe 1996; Gao et al. 1993). While reflected energy from midlevel water clouds may contaminate ice cloud signatures in the 1.38-μm channel, the frequency of occurrence of these clouds, on a global basis, appears to be significantly smaller than that of low-level water clouds (Henderson-

←

it detects neither if they are in the same pixel, as seen in the lower-left corner. (c) Phase of 44 620 pixels detected uniquely by the BSRR(3.7a/0.6) test) [C(1)] can only be confirmed over vegetated land and ocean areas for pixels that fail the BSRR(0.9/0.6) test for water clouds. Only 2063 pixels, shown in panel C(2), passed both tests and must be considered ambiguous. The remaining cloudy pixels are considered unambiguous and entered into the ice cloud-top phase analysis.

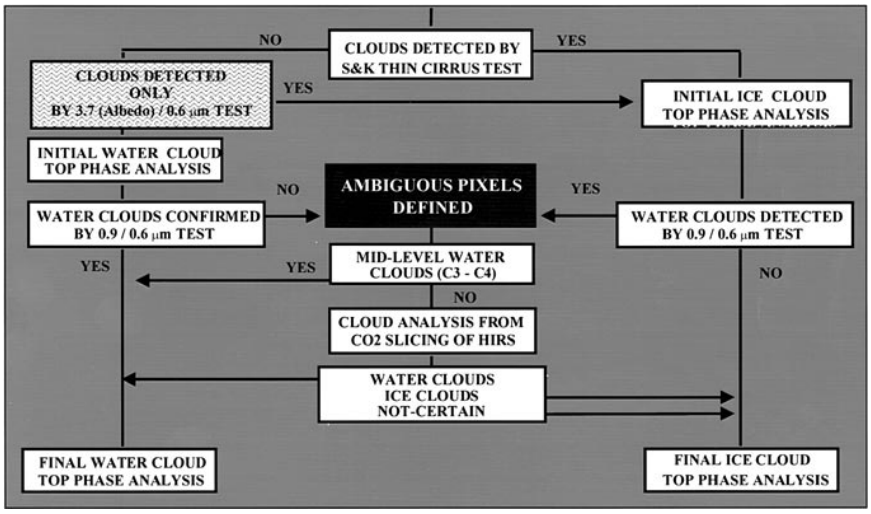

FIG. 4. Modified cloud-top phase algorithm for use with 3.7-μm data (with or without 1.6-μm data) for improved detection of thin cirrus clouds over vegetated land and water backgrounds.

Sellers 1986). Additionally, the 3.7-μm minus 10.8-μm BTD feature confirms the presence of middle-level water clouds. Thus, the 1.38-μm imagery should be an asset both for thin cirrus detection and discriminating between ice and water cloud-top phase. These topics will be more fully evaluated after the launch of a Moderate Resolution Imaging Spectroradiometer (MODIS), which carries the 1.38-μm channel in addition to other AVHRR/3 spectral bands.

Over more highly reflective surfaces in the 1.6-μm channel, the task of accurately classifying cloud-top phase becomes more difficult with the BSRR(1.6/0.6) test since values generally exceed unity for most surfaces. Table 1 shows typical albedos for various surfaces in the 1.6-μm band along with those for the 0.6- and 0.9-μm channels (Littesand and Kiefer 1987).

The difficulty of using the 1.6-μm data for cloud-top phase classifications over areas of highly reflective surfaces in the 1.6-μm band is demonstrated in the analysis of another AVIRIS scene, shown in Fig. 8, which was collected over Coffeyville, Kansas, in December 1990 (Hutchison and Choe 1996). Panels A(1) and A(2) show the 0.6- and 1.6-μm images of the scene, while thin cirrus can be seen to cover most of the area in the 1.38-μm band contained in panel B(1). Panel B(2) shows all cloud-free and cloudy pixels in the scene that satisfy the condition BSRR(1.6/0.6) $>$ 1.0. Unlike the results shown in panel C(2) of Fig. 6, all cirrus cloudy pixels in the scene fail the test criteria, for example, BSRR(1.6/0.6) $<$ 0.7, used to confirm the presence of cirrus clouds over low albedo surfaces except for those occurring over the river, [seen in panel B(2) of Fig. 8] smaller bodies of water such as lakes, and areas in and around the town in the upper-right corner of the scene.

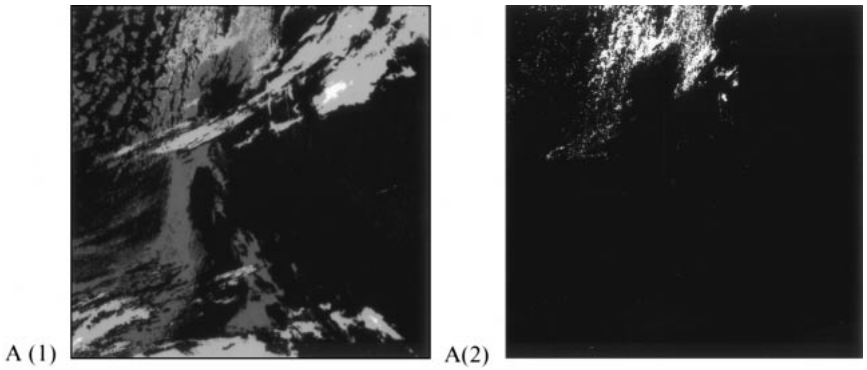

FIG. 5. Water clouds that were detected by the thin cirrus test and are present in the initial ice cloud-top phase analysis. Initial (ice and water) cloud-top phase analyses [A(1)] are based upon algorithm described in Fig. 1 (white are ice clouds with $T_{10.8} \leq -40$°C, light gray are clouds detected by the thin cirrus test, dark gray are assigned as water clouds, and cloud-free pixels are black). Water clouds detected by the thin cirrus test are shown in A(2).

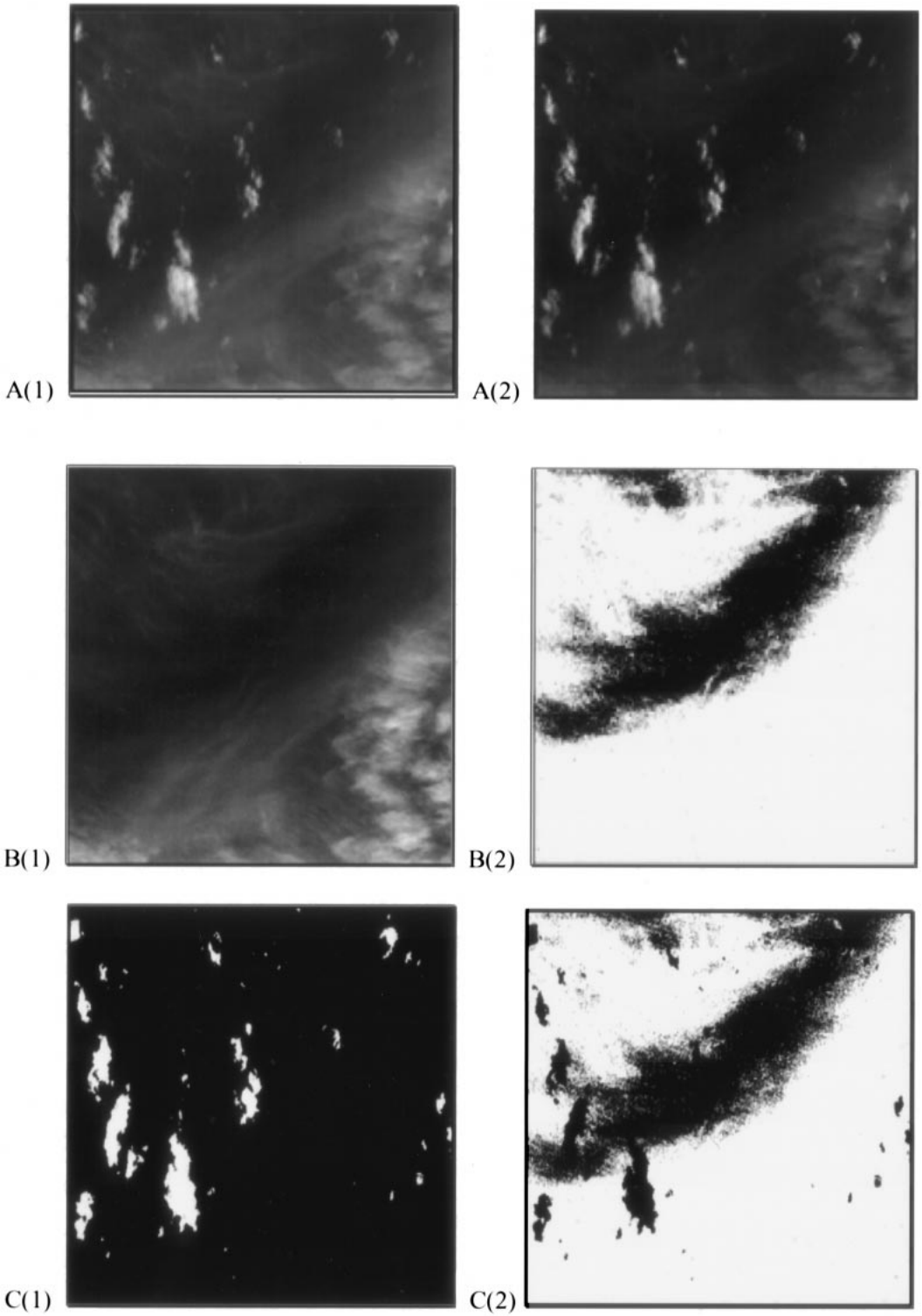

FIG. 6. Cloud-top phase classification using 1.6-μm imagery over low albedo (ocean) surface. (a) AVIRIS images in the 0.6-μm band [A(1)] and 1.6-μm band [A(2)] show areas of thin cirrus over lower-level water clouds. (b) The extent of thin cirrus is most clearly seen in the 1.38-μm band [B(1)], where reflected energy from lower-level water clouds is absorbed by water vapor in the scene. The manual ice cloud-top phase analysis is shown in B(2). (c) The automated water cloud-top phase analysis [C(1)] satisfies the criteria $0.7 < \text{BSRR}(1.6/0.6) < 1.0$ for all cloudy pixels in the scene, while ice cloud-top phase [C(2)] is analyzed under the condition $\text{BSRR}(1.6/0.6) < 0.7$ for the solar illumination and scattering geometry associated with this scene.

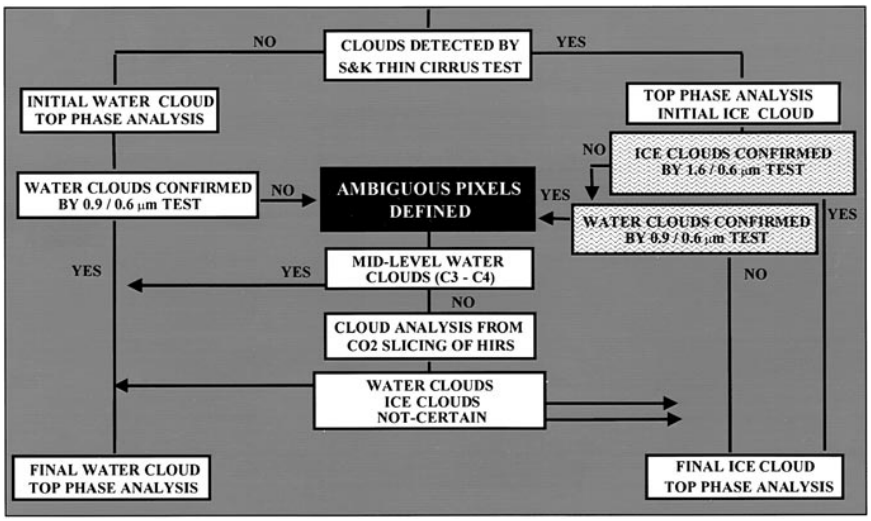

FIG. 7. Recommended procedure for enhanced cloud-top phase analyses in daytime AVHRR/3 imagery using the 1.6-μm imagery collected over low (1.6 μm) albedo surfaces.

Panel C(1) shows cloudy pixels with BSRR(1.6/0.6) values that lie in the 0.7–1.0 range, which is expected of water clouds as noted earlier for this solar illumination and scattering geometry. The ice cloud-top phase analysis, at panel C(2), is obtained by subtracting the analyses in panel C(1) from the total cloud/no-cloud analysis generated by the automated cloud detection algorithm, which is not shown but is very similar to that seen in panel B(1). All pixels contained in the ice cloud-top phase analysis in panel C(2) have BSRR(1.6/0.6) values larger than 1.0 because the albedo of land backgrounds in the 1.6-μm band generally exceeds that of the 0.6-μm channel, as seen in Table 1.

It is evident from Table 1 and results shown in Fig. 8 that the presence of thin cirrus cannot be confirmed using 1.6-μm data collected over most land surfaces. Consequently, ice cloud-top phase must again be inferred from the absence of water clouds using the BSRR(1.6/0.6) test in conjunction with the cloud/no-cloud mask generated by the automated cloud detection algorithm. This means that a primary objective for using 1.6-μm imagery in the cloud-top phase algorithm, which is to identify the pixels containing water clouds that were detected by the thin cirrus test and remove them from the initial ice cloud-top phase analysis, cannot be satisfied.

The recommended implementation for the use of 1.6-μm data collected over higher (1.6 μm) albedo surfaces in the cloud-top phase algorithm is shown in Fig. 9. The procedure would check for the presence of water clouds in the cloud/no-cloud mask generated from the automated cloud detection algorithm. If water clouds are not detected, cirrus clouds are referred. If water clouds are detected, there still remains the possibility that thin cirrus may be present above the water clouds. Therefore, pixels identified as containing water clouds must be considered ambiguous and be evaluated with cloud-top pressure analyses from the CO_2 slicing of HIRS/3 data.

TABLE 1. Typical albedos for common surfaces at wavelengths centered near AVHRR/3 channels (Littesand and Kiefer 1987).

Feature	0.6-μm albedo	0.9-μm albedo	1.6-μm albedo
Ocean	5%	0	0
Vegetated land	10%	50%	35%
Bare soil	25%	30%	50%

4. Conclusions

The primary goal of the automated cloud-top phase algorithm is the accurate identification and classification of ice and water clouds as an intermediate step in the analysis of remotely sensed cloud-top temperatures, pressures, and heights. If the phase of cloud tops analyzed in AVHRR/3 imagery can be determined with sufficient accuracy, the resultant cloud-top temperatures can be used as a constraint in the analysis of AMSU-B data. This approach has been shown to improve the accuracy of retrieved moisture profiles with DMSP SSM/T-2 data and may assist in the retrieval of cloud-base heights.

The task of creating accurate cloud-top temperature analyses is complicated by the presence of optically thin cirrus clouds, which allow energy from below to pass unattenuated to space. Thus, it is imperative that cloud-top phase analyses identify all ice clouds present in the imagery. Since both ice and water clouds lack a unique spectral signature in any subset of existing AVHRR/2 channels, a new methodology has been developed for the analysis of cloud-top phase that exploits the spectral signatures of ice and water clouds in the AVHRR/2 imagery and resolves ambiguities with cloud-top pres-

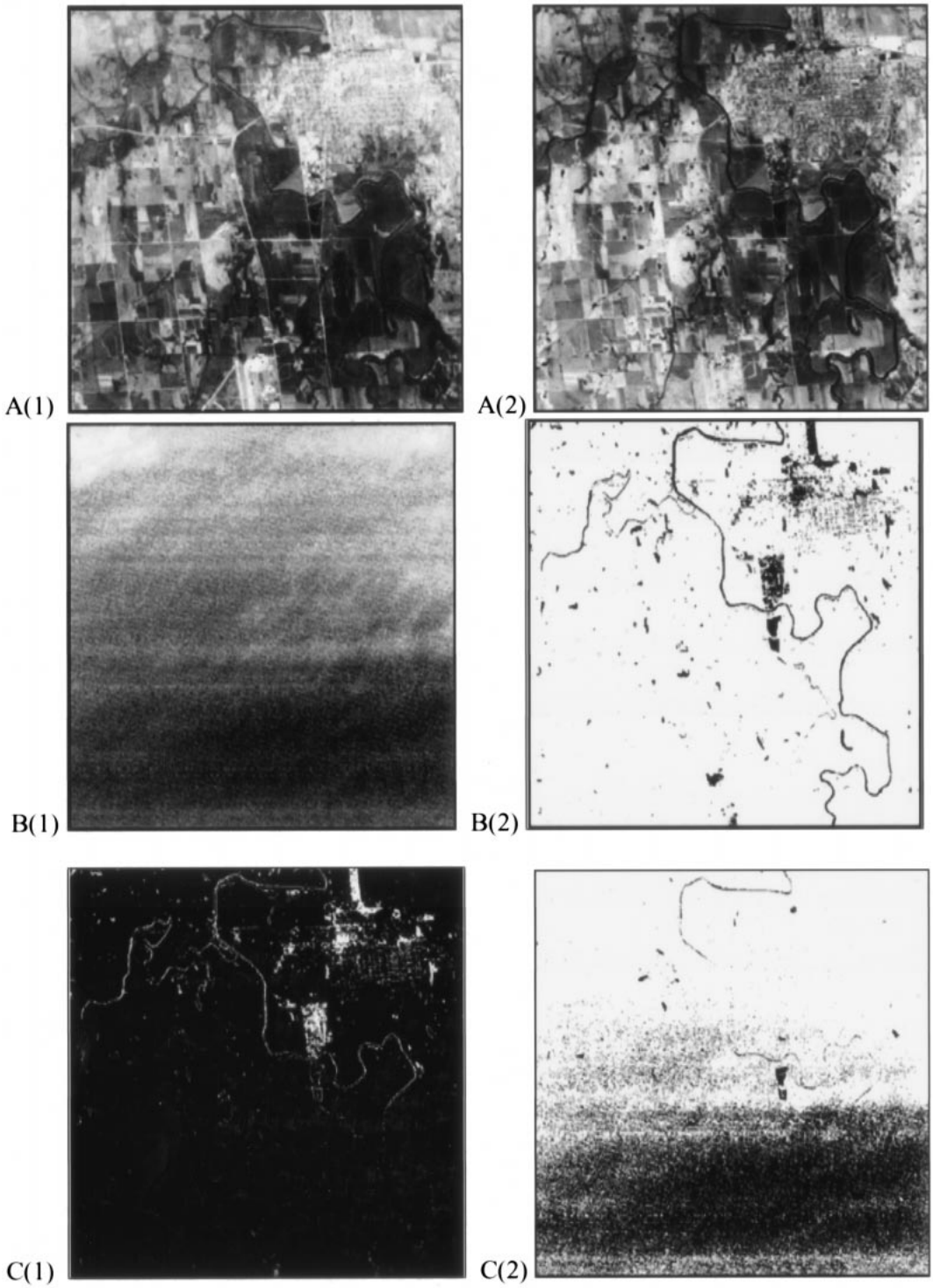

FIG. 8. Cloud-top phase classification of AVIRIS imagery collected over Coffeyville, KS, in Dec 1990. (a) AVIRIS imagery in the 0.6-μm band is contained in A(1), while data in the 1.6-μm band are shown in panel A(2). (b) The scene contains a large amount of very thin cirrus, as seen in the 1.38-μm band [B(1)], while B(2) shows all pixels satisfying criteria, BSRR(1.6/0.6) $>$ 1.0. (c) Pixels classified as water clouds in C(1) satisfy the criteria that $0.7 <$ BSRR(1.6/0.6) $<$ 1.0, while the ice phase analysis [C(2)] can only be inferred by the difference between the cloud/no-cloud mask used to initialize the cloud-top phase algorithm and the water cloud analysis.

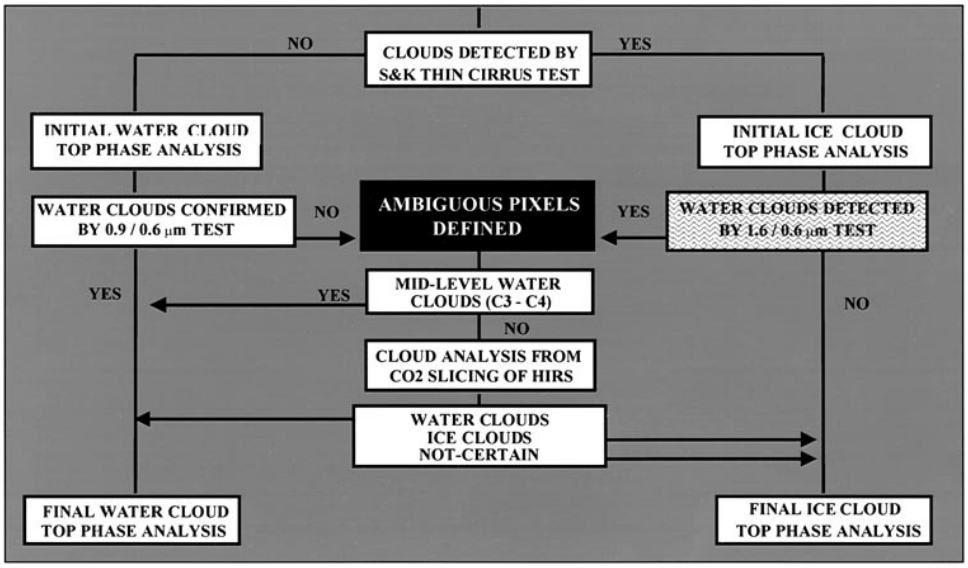

FIG. 9. Recommended procedure for enhanced cloud-top phase analyses in daytime AVHRR/3 imagery using the 1.6-μm imagery collected over higher (1.6 μm) albedo surfaces.

sure analyses derived from the CO_2 slicing of HIRS sounder data. While results of this new data fusion algorithm have been encouraging, some difficulties remain that make it highly desirable to reduce the number of pixels with ambiguous cloud phase signatures in the AVHRR imagery, which must be resolved with cloud-top pressure analyses. Additionally, the accurate detection of optically thin cirrus clouds remains problematic over land surfaces with existing AVHRR/2 data.

Earlier research suggested that a derived 3.7-μm albedo channel might be useful to improve the capability of detecting optically thin cirrus clouds in daytime imagery. This study confirms that very thin cirrus can be detected using the 3.7-μm albedo channel in conjunction with the 0.6-μm band over vegetated land and water backgrounds. However, the 3.7-μm albedo channel is not useful for detecting thin cirrus over sparsely vegetated land surfaces, which are too highly reflective in the derived 3.7-μm albedo channel. Additionally, the BSRR(3.7a/0.6) test is ineffective in identifying either ice or water clouds when they occur in the same pixel, although these cloud systems may be detected with the thin cirrus test. Consequently, the BSRR(3.7a/0.6) test is a complement to, not a replacement for, the thin cirrus test and the $T_{10.8} \leq -40$°C test. Finally, the phase of thin cirrus clouds that are uniquely detected by the BSRR(3.7a/0.6) test may be inferred as ice clouds, if the BSRR(0.9/0.6) test fails to detect the presence of optical thicker (water) clouds.

Initial results reveal that the utility of the 1.6-μm imagery is a function of the surface albedo in this band. When the albedos are small in the 1.6-μm channel, these data can be used to improve the specification of ice cloud-top phase analyses. Over backgrounds with larger albedos in the 1.6-μm band, the utility of these data is impacted by reflected energy from both densely vegetated and sparsely vegetated surfaces that tend to overwhelm the signature of ice clouds in this channel. Thus, over most land surfaces, ice clouds cannot be directly identified using 1.6-μm imagery but must be inferred by the absence of water clouds in the cloud/no-cloud mask generated by the automated cloud detection algorithm, which is used to initialize the automated cloud-top phase algorithm. Unfortunately, the confirmation of water clouds with bispectral tests that use the 0.9-, 1.6-, or 3.7-μm albedo channels in conjunction with the 0.6-μm band does not mean the absence of ice clouds in the AVHRR sensor field of view. Pixels in which water clouds are detected, using bispectral reflectance ratios, remain ambiguous and must undergo further testing to ensure that both ice and water clouds are not both present. Thus, a primary objective for the using 1.6-μm imagery in the cloud-top phase algorithm, which is to identify the pixels containing water clouds that were detected by the thin cirrus test and remove them from the initial ice cloud-top phase analysis, cannot be satisfied with these data and additional spectral data are needed to further resolve ambiguities. Likely candidates are the 1.38-μm band, which can suppress spectral signatures from low-level water clouds, and the 8.5-μm data (Ackerman et al. 1990). The use of these data for cloud-top phase classifications will be evaluated more fully in the near future after the launch of the MODIS sensor.

Currently, NOAA plans to interchange the 1.6- and 3.7-μm channels in the AVHRR/3 data transmission stream, which would not make both available at the same time. In addition to evidence presented here, the 3.7-μm data have been shown to be invaluable for discriminating between ice clouds and snow-covered sur-

faces, while the 1.6-μm channel is more useful for differentiating between water clouds and snow in an automated cloud detection algorithm. Additionally, 1.6-μm imagery are useful to confirm the presence of thin cirrus clouds over low (1.6 μm) albedo surfaces. While hardware and software considerations may preclude the transmission of all six channels during the AVHRR/3 era, it should be possible to further improve both cloud detection and cloud-top phase classifications if the 1.6-μm data were received together with imagery currently available from the AVHRR/2 sensor.

REFERENCES

Ackerman, S. A., W. L. Smith, and H. E. Revercomb, 1990: The 27–28 October 1986 FIRE IFO cirrus case study: Spectral properties of cirrus clouds in the 8–12 micron window. *Mon. Wea. Rev.*, **118,** 2377–2388.

Allen, R. C., P. A. Durkee, and C. H. Wash, 1990: Snow/cloud discrimination with multispectral satellite measurements. *J. Appl. Meteor.,* **29,** 994–1004.

d'Entremont, R. P., L. W. Thomason, and J. T. Bunting, 1987: Color composite image processing for multispectral meteorological satellite data. *Proc. SPIE,* **846,** 96–106.

DMSP, 1991: Block 6 Risk Reduction Contract Number F04701-91-C-0068, Appendix B. USAF Headquarters Space Systems Division, Los Angeles, CA, 21 pp.

Gao, B. C., A. F. H. Goetz, and W. J. Wiscombe, 1993: Cirrus cloud detection from Airborne Imaging Spectrometer Data using the 1.38 micron water vapor band. *Geophys. Res. Lett.,* **20,** 301–304.

Gutman, G. G., 1992: Satellite daytime image classification for global studies of Earth's surface parameters from polar orbiters. *Int. J. Remote Sens.*, **13,** 209–234.

Henderson-Sellers, A., 1986: Layer cloud amounts for January and July 1979 from 3D-Nephanalyses. *J. Climate Appl. Meteor.,* **25,** 118–132.

Huang, H. L., and K. D. Hutchison, 1998: The application of cloud-free radiances to the retrieval of cloud top pressures from HIRS data. *Proc. Ninth Conf. on Satellite Meteorology and Oceanography,* Paris, France, Amer. Meteor. Soc., 204–207.

Hutchison, K. D., and P. Janota, 1989: Cloud models enhancement project analysis phase report. Tech. Rep. TR-5773-1, The Analytic Sciences Corporations, 63 pp.

——, and K. Hardy, 1995: Threshold functions for automated cloud analysis of global meteorological satellite imagery. *Int. J. Remote Sens.,* **16,** 3665–3680.

——, and N. Choe, 1996: Application of 1.38-μm imagery for thin cirrus detection in daytime imagery collected over land surfaces. *Int. J. Remote Sens.,* **17,** 3325–3342.

——, and J. K. Locke, 1997: Snow identification through cirrus cloudy atmospheres using AVHRR daytime imagery. *Geophys. Res. Lett.,* **24,** 1791–1794.

——, K. Hardy, and B. C. Gao, 1995: Improved detection of optically thin cirrus clouds in nighttime multispectral meteorological satellite imagery using total integrated water vapor information. *J. Appl. Meteor.* **34,** 1161–1168.

——, B. J. Etherton, and P. C. Topping, 1997a: Validation of automated cloud top phase algorithms: Distinguishing between cirrus clouds and snow in a-priori analyses of AVHRR imagery. *Opt. Eng.,* **36,** 1727–1737.

——, ——, ——, and A. H. L. Huang, 1997b: Cloud top phase determination from the fusion of signatures in daytime AVHRR imagery and HIRS data. *Int. J. Remote Sens.,* **18,** 3245–3262.

Karlsson, K.-G., and E. Liljas, 1990: The SMHI model for cloud and precipitation analysis of multispectral AVHRR imagery. *SMHI Promis-Rapporter,* **10,** 74 pp.

Littesand, T. M., and R. W. Kiefer, 1987: *Remote Sensing and Image Interpretation*. 2d ed. Wiley and Sons, 721 pp.

Menzel, P., and K. Strabala, 1997: MODIS: Cloud top properties and cloud phase. MODIS Algorithm Theoretical Basis Document ATBD-04, 55 pp. [Available online at http://eospso.gsfc.nasa.gov/atbd/modistables.html.]

NPOESS, 1997: National Polar-Orbiting Operational Environmental Satellite System (NPOESS) Sensor Requirements Document (SRD) for the Visible/Infrared Imager/Radiometer Suite (VIIRS), NPOESS Integrated Program Office, 100 pp. [Available online at http://npoesslib.ipo.noaa.gov/ls_viirs.html.].

Ou., S. C., K. N. Liou, W. M. Gooch, and Y. Takano, 1993: Remote sensing of cirrus cloud parameters using AVHRR 3.7 and 10.9 mm channels. *Appl. Opt.,* **32,** 2171–2180.

——, and Coauthors, 1995: Remote sounding of cirrus cloud optical depths and ice crystal sizes from AVHRR data: Verification using FIRE-III-IFO measurements. *J. Atmos. Sci.,* **52,** 4143–4158.

——, K. N. Liou, and B. A. Baum, 1996: Detection of multilayer cirrus cloud systems using AVHRR data: Verification based on FIRE-III-IFO composite measurements. *J. Appl. Meteor.,* **35,** 178–191.

Rao, N. X., S. C. Ou, and K. N. Liou, 1995: Removal of solar component in the AVHRR 3.7-μm radiances for the retrieval of cirrus cloud parameters. *J. Appl. Meteor.,* **34,** 482–499.

Saunders, R. W., and K. T. Kriebel, 1988: An improved method for detecting clear sky and cloudy radiances from AVHRR data. *Int. J. Remote Sens.,* **9,** 123–150.

Scorer, R. S., 1990: *Satellite as Microscope*. Ellis Horwood Ltd., 268 pp.

Vane, G., 1987: Airborne visible/infrared imaging spectrometer (AVIRIS). Jet Propulsion Laboratory Publication 87-38, 97 pp.

Wilheit, T. T., and K. D. Hutchison, 1997: Water vapor profile retrievals from SSM/T-2 data constrained by infrared-based cloud parameters. *Int. J. Remote Sens.,* **18,** 3263–3278.

——, and ——, 1998: Cloud base height retrieval from DMSP microwave data and a priori cloud top temperatures. *Proc. Ninth Conf. Satellite Meteorology and Oceanography,* Paris, France, Amer. Meteor. Soc., 244–245.

——, and ——, 1999: Retrieval of cloud base heights from passive microwave and cloud top temperature data. *IEEE Trans. Geosci. Remote Sens.,* in press.

——, ——, and K. R. Hardy, 1994: A water vapor profiling algorithm for advanced environmental monitoring satellites. *Proc. Seventh Conf. Satellite Meteorology and Oceanography,* Monterey, CA, Amer. Meteor. Soc., 528–531.

Wrublewski, T. E., 1996: Overview of changes with the NOAA-K polar environmental satellite and their effects on users. *Proc. Fourth Int. Satellite Direct Broadcast Services Symp. for NOAA POES Users,* Anapolis, MD, NOAA.

Wylie, D. P., W. P. Menzel, H. M. Woolf, and K. I. Strabala, 1994: Four years of global cirrus cloud statistics using HIRS. *J. Climate,* **7,** 1972–1986.